Journal of the European Ceramic Society 45 (2025) 117597

Contents lists available at ScienceDirect

Journal of the European Ceramic Society

journal homepage: www.elsevier.com/locate/jeurceramsoc

Guided phase transition from TiO_2 rutile to anatase during electroforming of memristor-like devices

Andrea Alessio [a], Valentina Bonino [b], Federico Picollo [a], Lorenzo Mino [c], Matteo Fretto [d], Jorge Serrano [e], Vanessa Hinojosa-Chasiquiza [e], Kalle Goß [f], Regina Dittmann [f], Gema Martinez-Criado [b,g], Marco Truccato [a,*]

[a] Department of Physics, Interdepartmental Centre NIS, University of Torino, via P. Giuria 1, Torino I-10125, Italy
[b] European Synchrotron Radiation Facility, 71 Avenue des Martyrs, Grenoble 38043, France
[c] Department of Chemistry, Interdepartmental Centre NIS and INSTM, University of Torino, via P. Giuria 7, Torino I-10125, Italy
[d] INRIM, National Institute for Metrological Research, Strada delle Cacce 91, Torino I-10135, Italy
[e] GdS Optronlab, Universidad de Valladolid, Ed. LUCIA, Paseo de Belén 19, Valladolid 47011, Spain
[f] Peter Gruenberg Institute – Electronic Materials (PGI-7), Forschungszentrum Juelich GmbH and JARA-FIT, Juelich 52425, Germany
[g] Instituto de Ciencia de Materiales de Madrid (ICMM), Consejo Superior de Investigaciones Científicas (CSIC), Cantoblanco 28049, Spain

ARTICLE INFO

Keywords:
Submicron XANES
Micro-Raman
Memristor
Joule heating
Electric discharge
TiO_2
Rutile to anatase conversion

ABSTRACT

The effect of X-ray nano-beam irradiation has been investigated, along with a subsequent electric discharge between the metallic electrodes of memristive-like devices fabricated on top of rutile single crystals. X-ray irradiation with a photon flux of about 6×10^{12} photons/second impinging on an area of 74×60 nm^2, and with irradiation times of the order of tens of seconds per point, has been able to pattern a conducting path between the electrodes, which has guided the electric discharge process. The results from Ti K-edge XANES mapping with submicron spatial resolution show small changes in the configuration of the pre-edge peaks, suggesting the presence of anatase phase in the affected region, which is also confirmed by micro-Raman mapping. This implies the occurrence of very intense Joule heating during the electric discharge ($T > 2140$ K), followed by a very quick cooling process. This conversion of rutile to anatase represents a novel electrical method for the formation of localized anatase nanoparticles from rutile single crystals, which may be of help for specific applications.

1. Introduction

Memristive devices have recently attracted a lot of interest for non-volatile memory applications, mostly favored by their low power consumption, high switching speed, fabrication procedures compatible with CMOS technology and at low costs, non-volatile nature, and simple two-terminal structure, allowing for great scalability and high integration density [1–3]. Indeed, memristive devices can be schematized as exhibiting two different states: a high resistance state (HRS) encoding a logical 0, and a low resistance state (LRS), which encodes a logical 1. These states are usually non-volatile, implying that the devices can be used as data storage [4].

Many different architectures have been explored so far in terms of the number and nature of both the electrical contacts and the core layers, but the most prevalent device scheme consists of a metal-insulator-metal (MIM) layer stack, with the intermediate insulating layer sandwiched between two asymmetric metallic electrodes: one of them provides an ohmic contact with the active layer, and the other one originates a Schottky barrier [5].

In redox-based memristors, the active layer is typically made of a polycrystalline or amorphous transition metal oxide, such as TiO_2, HfO_2 or Ta_2O_5 [6]. Various mechanisms have been proposed over the years for resistive switching, with a filamentary-type valence change mechanism (VCM) being the most frequently observed [7,8]. This mechanism is related to the release of oxygen from the lattice under the influence of the electric field, resulting in the formation of oxygen vacancies which cause, due to their donor character, a highly conducting region connecting the two electrodes. To induce such a filament in a pristine device for the first time, the active layer typically undergoes a so-called electroforming step, which consists in its exposure to very intense electric fields to promote oxygen vacancy migration to form the filament. This electroforming step is, essentially, a reversible local dielectric

* Corresponding author.
E-mail address: marco.truccato@unito.it (M. Truccato).

https://doi.org/10.1016/j.jeurceramsoc.2025.117597
Received 28 March 2025; Received in revised form 20 May 2025; Accepted 4 June 2025
Available online 4 June 2025

breakdown in the film. If its parameters are not controlled well enough or an irregularity in the device leads to anomalously high fields or temperatures, an irreversible breakdown might occur. This can also happen during device operation and is one of the most common reasons for VCM-based devices to fail.

Extensive investigation of these conducting filaments in TiO_2-based devices has reported different chemical compositions, showing that most of the time they consist of a reduced TiO_x phase [9–11], but also that this phase can be surrounded by an anatase layer [11] or collapse into a Ti_4O_7 Magneli phase, when long-range oxygen vacancy order takes place [12,13]. Moreover, *operando* measurements have shown that the size of the filaments and their position with respect to the metal contacts can vary from cycle to cycle [14].

All these features are essential for understanding both the switching mechanism and possible device failure processes. For example, thermal cross-talking between adjacent devices has been highlighted as a potential issue, especially with the view to future, densely integrated memristor architectures, suggesting the need for specific techniques to design the thermal conductance of the filament-to-contact interface in such a way as to confine the heating as much as possible [15]. So far, the maximum temperatures reported for a filament have been estimated around 1000–1300 K [9,15], but a better knowledge of these values and their governing parameters (e.g. the values of the defect concentration or of the filament diameter) is definitely needed to gain control of the fabrication processes at the atomic scale and to achieve fabrication of reliably switching devices [16].

Finally, it has also been recently reported that TiO_2 irradiation by means of a synchrotron X-ray nanobeam is able to locally generate oxygen vacancies and to pattern a conductive filament that guides the electroforming process in the desired position, which can be defined as a kind of X-ray nanopatterning (XNP) [17–19]. The present work aims at exploiting this novel possibility by using some state-of-the-art spectroscopic instruments and techniques to improve the knowledge of both the local changes induced in TiO_2 at the submicrometer level and of the maximum temperatures developed during a device failure. Elucidating the influences of thermal and electronic stress on the morphology and properties of TiO_2 is expected to provide some insight into both the electroforming process and the dielectric breakdown mechanisms of these devices.

2. Experimental

(110)-oriented TiO_2 rutile single crystals (Shinkosha Co., Ltd., Japan) were annealed at 300°C in H_2 (4 %)/Ar atmosphere for 2 h, to introduce controlled oxygen vacancies and increase the sample conductivity. Then, metal electrodes were deposited on their top surfaces, with a 2 μm gap separating them (see Fig. 1a and 1b). The two electrodes are asymmetric, one consisting of 60 nm Pt, and the other of 30 nm Ta with a 30 nm Pt layer on top. Since Pt forms a Schottky barrier with rutile and Ta forms an ohmic contact, such an asymmetry of the electrodes is expected to result in a rectifying diode-like behavior [4]. Although this in-plane geometry does not correspond to the typical one used for memristive devices, it was chosen to allow the investigation of device electroforming and failure using XNP and spectroscopic techniques.

Samples were initially irradiated at the beamline ID16B of European Synchrotron Radiation Facility (ESRF) in Grenoble, France, in order to increase the local oxygen vacancy content and electrical conductivity so as to guide the electroforming process, as it has already been demonstrated in previous works by our group [17,18]. An area of $4 \times 3\ \mu m^2$ (H×V) was irradiated across the gap by raster scanning a $74 \times 60\ nm^2$ (H×V) nanobeam in 16-bunch pink beam mode with an energy of 17.5 keV and a flux of 6.13×10^{12} photons/second. The area was irradiated by exposing each point for 25 s and with a beam pitch of 200 nm in both directions, resulting in a total fluence of $1.16 \times 10^{13}\ J/m^2$ and in an absorbed dose of 5.16×10^{12} Gy.

Subsequently, I-V curves were acquired using a Keithley 6487 electrometer at progressively increasing voltages, until discharge processes led to the formation of a conducting filament connecting the two electrodes. Fig. 1c shows the typical I-V curves for a pristine device and after electroforming, with a difference of about 2 orders of magnitude in the resistance of these two states. This change is very similar to the one occurring during the electroforming step in the fabrication of TiO_2-based memristive devices. Of course, during the fabrication of memristors this process must be carefully controlled to achieve reversible resistance switch, by setting a suitable current compliance to avoid the formation of irreversible conducting filaments. In contrast, in our experiments the current compliance during the discharge was deliberately set to a high value (≈ 2.5 mA) in order to get a sufficiently large conducting filament to be investigated by means of XANES and Raman spectroscopy using micrometer-sized probes.

SEM imaging was performed with a Coxem EM30Plus microscope for both pristine samples and those after discharge.

X-Ray Fluorescence (XRF) measurements were performed for pristine devices at ID16B with a 17.5 keV beam $74 \times 60\ nm^2$ in size, and then repeated at ID21 after electroforming, with a beam energy of 5.1 keV, and a size of 800×400 (H×V) nm^2. XRF spectra were collected at each point of the maps and the intensity of the fluorescence lines was obtained for each of the elements in the sample. Fig. 1b shows the XRF map of a pristine sample corresponding to the sum of the Pt L and Ta L lines, in which both metal electrodes are clearly visible.

XANES mapping of the Ti K-edge (4966 eV) was performed at beamline ID21 of ESRF. Absorption spectra were collected in fluorescence mode between 4950.0 and 5039.6 eV by scanning the areas of interest with the $800 \times 400\ nm^2$ beam for each energy value, with a step size $\Delta E = 0.2$ eV. Above this edge, the X-ray attenuation length in TiO_2 is approximately 5.3 microns [20]. XANES spectra of two TiO_2 stoichiometric standards (rutile and anatase) were also acquired and are shown in Fig. 2. The possible presence of the brookite polymorph was not considered at this stage of the investigation.

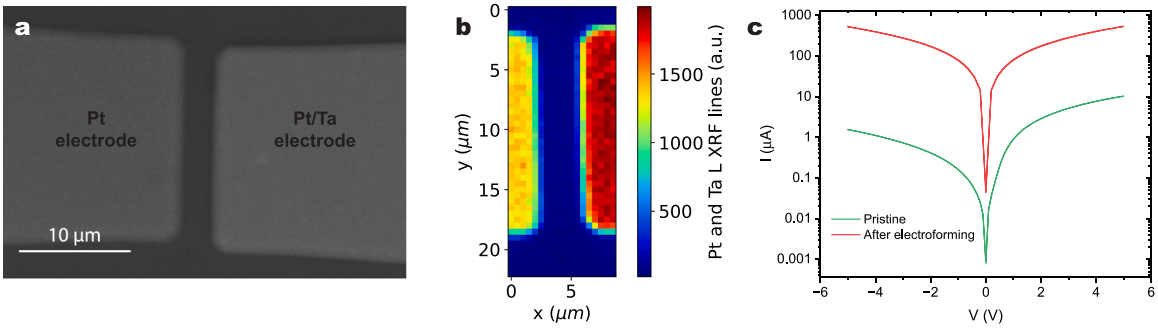

Fig. 1. A) SEM image of the pristine sample. B) XRF map of the pristine sample showing the sum of the signals related to Pt and Ta L lines, as measured at ID16B. C) I-V curves collected before (green line) and after (red line) electroforming.

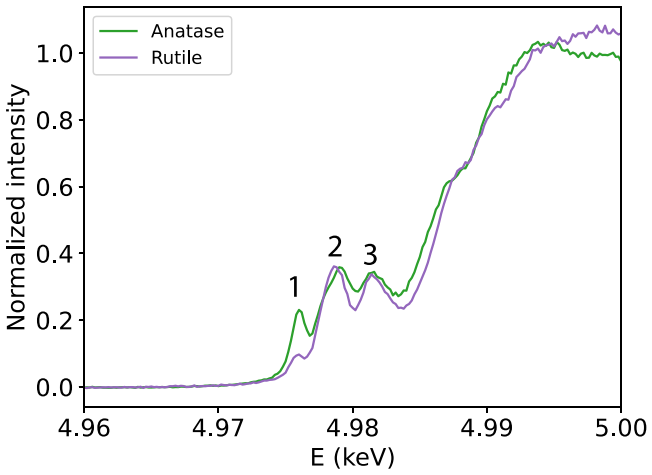

Fig. 2. XANES spectra of stoichiometric rutile and anatase standards.

Raman scattering imaging was performed at room temperature in the region of interest employing a HORIBA Soleil micro-spectrometer equipped with an excitation light of 532 nm and a UV/Vis/NIR Syncerity CCD detector Peltier-cooled at −60°C.

Maps were acquired with a step size of 1 × 1 μm^2, using a 100× HORIBA Plain Fluo objective with a working distance of 1 mm, a numerical aperture of 0.90, an acquisition time of 1 s per point, and a laser power of 0.57 mW. A grating of 2400 lines/mm centered at 400 nm and a hole diameter of 200 μm at the spectrometer entrance were employed to achieve an optimal signal-to-noise ratio with minimum imaging time at the largest spectral resolution. Autofocus on spectral signal was employed at each point of the map. The beam size for this imaging technique is limited by diffraction, allowing for a resolution of about 720 nm. The data processing included background subtraction, noise reduction through smoothing, and normalization of the peak intensities.

This analysis aimed at obtaining information about the vibrational modes of the sample surface layer, to be compared to the results of XANES mapping, which instead gives information on the local environment of Ti atoms in the bulk of the sample.

3. Results and discussion

The SEM image of a sample that underwent an electric discharge is shown in Fig. 3a. It is apparent that both electrodes have been severely damaged and delaminated, with the most severe damage occurring at the pure Pt contact. The appearance of the Pt/Ta electrode is like the one seen in other electroforming experiments, where metallic contacts locally melted (see for instance Figure 6 of Ref. [21]), but the most important feature is the appearance of a bump in the gap between the electrodes. Although technical problems with the focus distance at the stage of sample irradiation introduced an uncertainty of a few microns in the vertical alignment between the beam and the electrodes, the width of the filament (≈2.5 μm versus the 3 μm of the irradiated area) and evidence from previous works [17,18] make it very likely that the bump and the irradiated area coincide.

An XRF map of this sample was also collected after electroforming and is shown in Fig. 3b. The absence of any trace of Pt and Ta in the gap between the electrodes rules out the possibility of metal electromigration during the application of high electric fields in the discharge process.

Moreover, a XANES map 15 × 20 (H×V) μm^2 in size was acquired for the same sample, with a 1 μm step in both the horizontal and vertical directions. The map position with respect to the electrodes and the pixel size are shown in Fig. 3a, and a typical spectrum corresponding to a pixel is shown in Fig. 3c.

By looking at the XANES spectra of the rutile and anatase standards shown in Fig. 2, it is possible to see that the main difference between

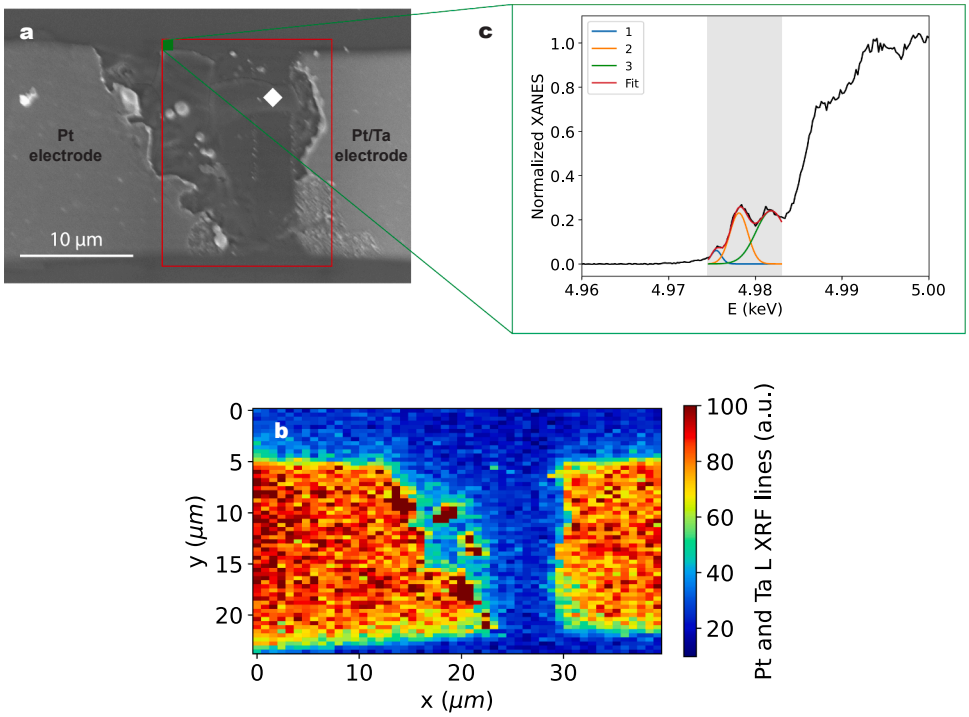

Fig. 3. A) SEM image showing a discharge region. The white diamond indicates the position of the bump connecting the two electrodes after electroforming. The red box highlights the extension of the XANES map, and the green solid square represents the pixel size of this map (to scale). B) XRF map of the same sample of panel (a) showing the sum of the signals related to Pt and Ta L lines. C) example of a XANES spectrum and fitting obtained for a single point of the map. Contributions from the peaks labelled as 1, 2, and 3 are represented by the cyan, orange and green Gaussian curves, respectively. The grey region shows the data region that was fitted. The red curve represents the total fitting of the model, and the black one represents experimental data.

them lies in the different relative amplitude of the pre-edge peaks labelled as 1 and 2. For this reason, we fitted the pre-edge peaks with three Gaussian functions

$$I(E) = \sum_{n=1}^{3} \frac{A_n}{\sigma_n \sqrt{2\pi}} e^{\left[-(E-E_{0n})^2 / 2\sigma_n^2\right]}$$

where A_n represents the amplitude, σ_n is the standard deviation, and E_{0n} the center of the curve corresponding to the n-th peak.

The application of this model to the rutile and anatase standards has resulted in the parameter values reported in Table I. An example of the corresponding fits is reported in Figure S1 of Supplementary Information.

These values confirm that the most important difference for the standards consists in the fact that the amplitude ratio A_1/A_2 is greater in anatase than in rutile, with a very significant increase of about 43 %. Moreover, there is also a statistically significant ($t(17) = 5.30105$, p-value $= 0.000029$) difference between the centers E_{02} of the second gaussian, with the center of anatase that lies at an energy value lower than the one of rutile by $\Delta E_{02} = 0.18$ eV. This result is probably counterintuitive when looking at Fig. 2, but can be explained by the stretching of the second peak towards higher energy values caused by the presence of the third peak at higher energies (see Figure S1).

The spectrum of each point of the XANES map was fitted with this model, as shown for example in Fig. 3c, and the corresponding maps were plotted for each of the parameters.

Fig. 4 shows the results of this pre-edge fitting procedure. In Fig. 4a the spatial distribution of the energy value E_{02} is shown, revealing a small shift towards lower energy values at the location of the box with 1 μm $\leq x \leq$ 14 μm and 3 μm $\leq y \leq$ 4 μm, where the electroformed filament lies. This is also confirmed by the vertical profile taken at $x = 8$ μm (see the blue line in Fig. 4c), where it is possible to notice that the E_{02} decrease by about 0.12–0.14 eV exceeds the uncertainty value. This shift agrees with the decrease of E_{02} observed in the anatase standard, suggesting the possible presence of the anatase phase in this region. However, it should be considered that, in the energy range of the fits, the penetration depth of X-rays (over 5 μm) is much greater than the thickness of the layer that has taken part in electroforming, which is typically of the order of 200 nm, as shown in previous work by our group [17] and also confirmed by AFM measurements of the present samples (see Figure S2 of Supplementary Material). This implies that in the electroformed region only approximately 7 % of the XANES signal originated from the TiO_2 volume where the electrical discharge occurred. Because of this situation, we cannot exclude that some component of the shift observed for this peak is due to the decrease in the Ti-apical O distance in the TiO_6 octahedra [22], which could be induced by the high density of defects created by the electrical discharge or by heavy irradiation in the bulk rutile underneath the electroformed layer. Concerning the type of defects, it has already been demonstrated that XNP of rutile generates oxygen vacancies, which are known to act as n-dopants and locally increase the electrical conductivity [18]. Therefore, the low resistance observed in the filament after electroforming represents a strong confirmation of their presence. As a final observation, it can also be noted that, even if the width of the filament matches reasonably well the size of the area irradiated at ID16B, its length (≈ 14 μm) largely exceeds the irradiated size (4 μm), indicating that the irradiation simply pinned an avalanche process that took place along the x-direction, which is also the direction of the current flow.

On the other hand, Fig. 4b shows the map of the ratio between the amplitudes of the pre-edge peaks 1 and 2 (i.e. the quantity A_1/A_2). An increase can be observed essentially in the same region where the decrease of E_{02} takes place (specifically, in the case of A_1/A_2, in the box with 1 μm $\leq x \leq$ 12 μm and 3 μm $\leq y \leq$ 4 μm). A vertical profile of the map taken at the same position of $x = 8$ μm (see the orange line in Fig. 4c) confirms that in correspondence with the filament position the value of this ratio is $A_1/A_2 \approx 0.21$, to be compared with an average value $A_1/A_2 \approx 0.15$, which implies that this increase is beyond the uncertainty.

Therefore, Fig. 4a and 4b jointly point to the presence of some anatase phase that has been formed during the electroforming process, most likely because of material melting due to a very intense Joule heating, and subsequent recrystallization. This is further confirmed by the rounded edges of the electroformed filament, as visible in Fig. 3a.

It is fair to say that these changes detected with XANES spectroscopy are very small, but this is consistent with the small contribution coming from the electroformed region, as has been explained above. However, this also implies that extracting more quantitative results from XANES spectroscopy is not feasible.

The results of Raman mapping are summarized in Fig. 5. Fig. 5a shows the SEM image of the sample with two reference points, which have been marked with numbers 1 and 2, respectively.

Point no.1 corresponds to a region of the sample with no shielding from metallic contacts and reasonably far from the conducting filament, so that it can be considered unaffected by the discharge process. Fig. 5b shows that the spectrum collected in this point consists of the rutile vibrational modes only, as expected, namely the E_g mode ($\nu \approx 450$ cm^{-1}) and the A_{1g} mode ($\nu \approx 610$ cm^{-1}), plus a broad band centered at $\nu \approx 250$ cm^{-1}, which is attributable to multi-phonon processes [23,24]. Looking at the spectrum collected at the location of the filament (point 2), the same vibrational modes of rutile are still visible, but an additional peak appears at $\nu \approx 140$ cm^{-1} (highlighted by the red line in Fig. 5b). This new peak can be attributed to the E_g mode of anatase TiO_2 [23,25]. On the other hand, the same spectrum shows no presence of the strongest peak of brookite TiO_2 ($\nu = 153$ cm^{-1}) [23]. This implies that no brookite is observable within the sensitivity limits of our Raman measurements, which also justifies *a posteriori* the fact that brookite has been neglected in the XANES measurements.

For systematic data analysis, we have selected as references three representative Raman spectra corresponding to anatase, rutile, and an electrode (for the last one, see Figure S3 in Supplementary Information). Then, the spectrum measured at each pixel has been fitted by means of a linear combination of these three references using the Classical Least Squares (CLS) method and obtaining the percentage contribution of each component.

The corresponding semi-quantitative map showing the most important contribution at each pixel is shown in Fig. 5c: By comparing it with the SEM image (Fig. 5a), it is possible to conclude that the presence of the anatase phase is localized in the conducting filament. Data acquired at the location of the metal electrodes are not significant, since no Raman signal was detected in these regions due to the shielding by the electrodes themselves (see Figure S3). This result confirms the findings of the XANES measurements about the presence of anatase TiO_2 in the conducting filament.

We can compare our findings with previous XANES measurements of the Ti K-edge performed on memristive devices fabricated with amorphous TiO_2 [26]. However, those measurements focused on possible changes in the Ti oxidation state and were not able to detect any difference related to resistance switching, since the oxidation state remained close to + 4 both before and after electroforming [26]. Our results are not in contradiction with this conclusion, since the phase transformation from rutile to anatase TiO_2 does not involve any change in Ti oxidation state. However, it should be noted that, in the geometry of that experiment, the expected diameter of the conducting filaments

Table I
Values of the ratio between the amplitude of peaks 1 and 2 (A_1/A_2), the position of the center of the second peak (E_{02}), and the number of spectra used for each determination, for the rutile and anatase standards, respectively.

	Rutile	Anatase
A_1/A_2	0.21 ±0.01	0.30±0.03
E_{02} (keV)	4.97888 ±0.00009	4.97870 ± 0.00009
Number of spectra	9	10

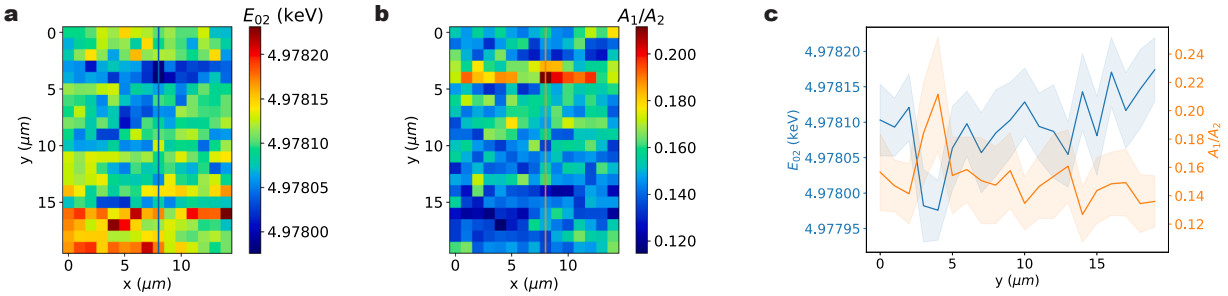

Fig. 4. A) Spatial distribution of the energy value E_{02} corresponding to the center of peak 2, and B) of the amplitude ratio A_1/A_2. C) profiles extracted from maps A) (blue line, left axis) and B) (orange line, right axis) along the vertical lines positioned at $x = 8$ μm. Shaded regions represent the error bars associated with each data point.

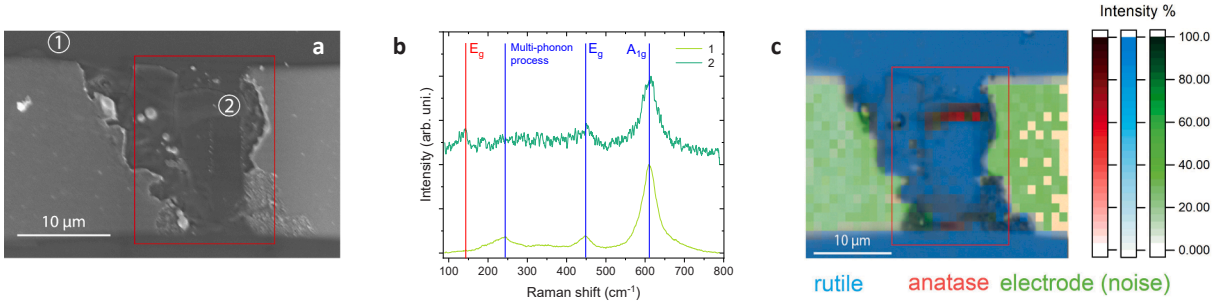

Fig. 5. A) SEM image of the region mapped with Raman spectroscopy. B) Raman spectra collected in points 1 and 2 of panel A): the peaks identified with blue vertical lines correspond to rutile TiO_2, whereas the peak marked with the red line corresponds to anatase TiO_2. C) intensity map showing the dominant component of the spectrum at each position according to the Classical Least Squares (CLS) method (see text). The color bars show the percentage of the dominant component in blue for rutile, in red for anatase and in green for the electrode; the red box shows the extension of the XANES map for comparison.

(of the order of 10 nm) was much less than the X-ray probe size (2 μm), so any signal from the amplitude ratio A_1/A_2 was most likely overwhelmed by the contribution of the unaffected amorphous phase TiO_{2-x}. This indicates that very careful experimental design and data analysis are necessary to detect such small changes in the XANES spectra of electroformed filaments.

Indeed, by using much smaller probe sizes (≈ 25–100 nm) and investigating the Ti L absorption edge in the region of soft X-rays, it has been possible to detect the formation of the anatase phase [11,12,27], or of the rutile plus reduced TiO_x phases [9], at the location of the electroformed filaments. However, in all of these cases, the device active layer consisted of *amorphous* TiO_{2-x}, which implied that the minimum local temperature necessary to generate the observed phases during electroforming was reported to be between 620 and 800 K in the case of anatase [11,12,27] or 1000 K in the case of rutile [9]. Similar temperatures values were also confirmed by *operando* Scanning Thermal Microscopy (SThM) direct measurements of the local temperature of individual conducting filaments, which pointed out a maximum value of over 500 K in the case of TiO_2–based devices [14], whereas for active layers consisting of HfO_2 temperatures as high as 1350 K were reported [15].

However, our experiment is different because, at the location of the conducting filament, we have detected recrystallization into the anatase phase starting from a TiO_2 *rutile single crystal*.

From the point of view of the local temperature, this implies that the electric discharge process has resulted in values exceeding the melting point of bulk rutile (approximately 2140 K, Ref. [28]), which is the highest value reported so far, to the best of our knowledge. This could have some implications for the design of heating dissipation routes in densely integrated systems, in order to limit the damage in case of failure.

On the other hand, our result is even more interesting from the point of view of phase transitions. Indeed, it is well-known that rutile cannot be converted into the anatase phase under steady-state conditions, due to the absence of any phase equilibrium in the thermodynamics of these systems. Therefore, a few peculiar methods have been developed to induce the rutile to anatase phase transition, which is sometimes desirable because of the better charge separation and ion storage properties of anatase. Most of these methods start with rutile thin films or nanoparticles, which are doped for example by means of ammonolysis [29] or oxygen ion implantation [30], and sometimes also involve thermal treatments in reducing atmospheres like H_2 [31] and NH_3 [32]. Other less conventional methods make use of strongly non-steady state conditions like acoustic shock waves [33] or pulsed laser irradiation [34,35]. In these cases, the mechanism responsible for the rutile to anatase phase transition stems from the fact that anatase has a lower liquid-to-solid interfacial energy, which corresponds to a smaller critical radius compared to the one of rutile, so that the anatase phase is preferentially nucleated in the molten state. When the cooling time of the liquid is very fast (from ns to ms, depending on the experimental details of the energy pulse delivered to the system) [33,35], the nuclei do not have enough time to grow into bigger grains and the liquid-like particles are solidified into small grains where the atoms are frozen in the thermodynamically metastable positions they were occupying, i.e. in the anatase phase.

It is very likely that something similar has occurred in our samples during the electric discharge process, whose duration can be estimated in the range of a few ms. Therefore, anatase is expected to be present in the electrically induced filaments in the form of nano-sized crystallites.

It is also worth noting that, among all the methods reported for rutile to anatase conversion, only laser irradiation refers to bulk rutile [34,35]. However, the intrinsic features of this method imply that a high spatial resolution (down to about 5 μm) can be obtained only at the cost of inducing local ablation in the crystal. Our findings show that another conversion method is available by inducing a local electric discharge in rutile, which can achieve a spatial resolution of about 2 μm and results

in a perturbation of a surface by 100–200 nm. This result could be of importance for specific applications requiring anatase nano-crystallites regularly arranged on a surface.

4. Conclusions

The formation of conducting filaments via electric discharge in single crystal TiO_2 rutile has been guided via XNP and analyzed by means of nano-XRF, submicron-XANES and micro-Raman imaging.

A careful analysis of the relative amplitude of the first two pre-edge peaks in the Ti K-edge XANES spectra has shown the presence of anatase phase at the location of the conducting filament. A small displacement in the energy position of the second pre-edge peak has also been detected, which agrees with the formation of anatase but could also be related to a distortion of the TiO_6 octahedra associated with the filament. These findings have also been confirmed via Raman imaging, which detected the anatase phase in the conducting filament only.

Therefore, these results have proved that anatase nanocrystals are formed during electric discharge in a single crystal rutile matrix, which implies an unprecedented Joule heating over 2140 K, that triggers local melting with subsequent recrystallization processes.

This electric discharge represents a novel method to induce a localized rutile to anatase phase transition in a bulk crystal, providing a better spatial resolution compared to laser irradiation.

CRediT authorship contribution statement

Gema Martinez-Criado: Writing – review & editing, Writing – original draft, Validation, Supervision, Resources, Conceptualization. **Kalle Goß:** Writing – review & editing, Writing – original draft, Methodology, Investigation. **Regina Dittmann:** Validation, Supervision, Resources, Investigation, Conceptualization. **Vanessa Hinojosa-Chasiquiza:** Writing – original draft, Visualization, Methodology, Investigation, Formal analysis. **Jorge Serrano:** Visualization, Supervision, Resources, Methodology, Investigation, Formal analysis. **Matteo Fretto:** Methodology, Investigation, Formal analysis. **Lorenzo Mino:** Writing – review & editing, Validation, Supervision, Methodology, Investigation, Formal analysis, Conceptualization. **Federico Picollo:** Validation, Methodology, Investigation, Conceptualization. **Valentina Bonino:** Writing – review & editing, Validation, Resources, Methodology, Investigation, Data curation, Conceptualization. **Andrea Alessio:** Writing – review & editing, Writing – original draft, Visualization, Validation, Software, Investigation, Formal analysis, Conceptualization. **Marco Truccato:** Writing – review & editing, Writing – original draft, Supervision, Project administration, Investigation, Funding acquisition, Conceptualization.

Declaration of Competing Interest

The authors declare that they have no known competing financial interests or personal relationships that could have appeared to influence the work reported in this paper.

Acknowledgements

The authors acknowledge the ESRF for the beamtime allocated on the beamlines ID16B and ID21 (experiment MA-4883) and the valuable help by Eduardo Villalobos during data acquisition at ID21. A.A. and M. T. acknowledge partial support from the “Departments of Excellence” (L. 232/2016) grant, funded by MIUR, and from the project HiFluXTech, jointly funded by Compagnia di San Paolo and University of Torino. J. S. and V. H.-C. acknowledge fruitful discussions with J. Jiménez and I. Mediavilla in the early stages of this work, and financial support through grants PID2021-126046OB-C22 funded by MCIN/AEI and TED2021-130786B-I00 funded by MTED/AEI; both also funded by 10.13039/501100011033/FEDER, EU. The micro-Raman imaging instrument was granted by JCYL Infrared call IR2019-UVA09 also funded by FEDER, EU. K.G and R.D. acknowledge the German Science Foundation (DFG) for funding within the project SFB 917 (Nanoswitches).

Appendix A. Supporting information

Supplementary data associated with this article can be found in the online version at doi:10.1016/j.jeurceramsoc.2025.117597.

References

[1] D.B. Strukov, D.R. Stewart, J. Borghetti, X. Li, M. Pickett, G.Medeiros Ribeiro, W. Robinett, G. Snider, J.P. Strachan, W. Wu, Q. Xia, J.Joshua Yang, R.S. Williams, Hybrid cmos/memristor circuits. Proc. IEEE International Symposium on Circuits and Systems, ISCAS, 10 Paris, France, 2010, pp. 1967–1970.

[2] H.Y. Lee, Y.S. Chen, P.S. Chen, T.Y. Wu, F. Chen, C.C. Wang, P.J. Tzeng, M.J. Tsai, C. Lien, Low-power and nanosecond switching in robust hafnium oxide resistive memory with a thin ti cap, IEEE Electron Device Lett. 31 (1) (2010) 44–46, https://doi.org/10.1109/LED.2009.2034670.

[3] M.J. Lee, C.B. Lee, D. Lee, S.R. Lee, M. Chang, J.H. Hur, Y.B. Kim, C.J. Kim, D. H. Seo, S. Seo, U.I. Chung, I.K. Yoo, K. Kim, A fast, high-endurance and scalable non-volatile memory device made from asymmetric Ta_2O_{5x}/TaO_{2x} bilayer structures, Nat. Mater. 10 (8) (2011) 625–630.

[4] R. Waser, R. Dittmann, G. Staikov, K. Szot, Redox-Based resistive switching memories – nanoionic mechanisms, prospects, and challenges, Adv. Mater. 21 (25–26) (2009) 2632–2663, https://doi.org/10.1002/adma.200900375.

[5] D. Ielmini, Resistive switching memories based on metal oxides: mechanisms, reliability and scaling, Semicond. Sci. Technol. 31 (6) (2016) 063002, https://doi.org/10.1088/0268-1242/31/6/063002.

[6] R. Dittmann, J.P. Strachan, Redox-based memristive devices for new computing paradigm, APL Mater. 7 (11) (2019) 110903, https://doi.org/10.1063/1.5129101.

[7] W. Sun, B. Gao, M.F. Chi, Q.F. Xia, J.J. Yang, H. Qian, H.Q. Wu, Understanding memristive switching via in situ characterization and device modeling, Nat. Commun. 10 (1) (2019) 3453, https://doi.org/10.1038/s41467-019-11411-6.

[8] C. Baeumer, R. Valenta, C. Schmitz, A. Locatelli, T.O. Mentes, S.P. Rogers, A. Sala, N. Raab, S. Nemsak, M. Shim, C.M. Schneider, S. Menzel, R. Waser, R. Dittmann, Subfilamentary networks cause Cycle-to-Cycle variability in memristive devices, ACS Nano 11 (7) (2017) 6921–6929, https://doi.org/10.1021/acsnano.7b02113.

[9] D. Carta, A.P. Hitchcock, P. Guttmann, A. Regoutz, A. Khiat, A. Serb, I. Gupta, T. Prodromakis, Spatially resolved TiO_x phases in switched RRAM devices using soft X-ray spectromicroscopy, Sci. Rep. 6 (2016) 21525, https://doi.org/10.1038/srep21525.

[10] Y. Beilliard, F. Paquette, F. Brousseau, S. Ecoffey, F. Alibart, D. Drouin, Investigation of resistive switching and transport mechanisms of Al_2O_3/TiO_{2-x} memristors under cryogenic conditions (1.5 K), AIP Adv. 10 (2020) 025305, https://doi.org/10.1063/1.5140994.

[11] J.P. Strachan, D.B. Strukov, J. Borghetti, J. Joshua Yang, G. Medeiros-Ribeiro, R. Stanley Williams, The switching location of a bipolar memristor: chemical, thermal and structural mapping, Nanotechnology 22 (25) (2011) 254015, https://doi.org/10.1088/0957-4484/22/25/254015.

[12] J.P. Strachan, M.D. Pickett, J.J. Yang, S. Aloni, A.L.D. Kilcoyne, G. Medeiros-Ribeiro, R.S. Williams, Direct identification of the conducting channels in a functioning memristive device, Adv. Mater. 22 (32) (2010) 3573–3577, https://doi.org/10.1002/adma.201000186.

[13] S.H. Chang, J. Kim, C. Phatak, K. D'Aquila, S.K. Kim, J. Kim, S.J. Song, C.S. Hwang, J.A. Eastman, J.W. Freeland, S. Hong, X-ray irradiation induced reversible resistance change in $Pt/TiO_2/Pt$ cells, ACS Nano 8 (2) (2014) 1584–1589, https://doi.org/10.1021/nn405867p.

[14] T. Swoboda, X. Gao, C.M.M. Rosario, F. Hui, K.C. Zhu, Y. Yuan, S. Deshmukh, C. Koroglu, E. Pop, M.R. Lanza, H. Hilgenkamp, M.M. Rojo, Spatially-Resolved thermometry of filamentary nanoscale hot spots in TiO_2 resistive random access memories to address device variability, ACS Appl. Electron. Mater. 5 (2023) 5025–5031, https://doi.org/10.1021/acsaelm.3c00782.

[15] S. Deshmukh, M.M. Rojo, E. Yalon, S. Vaziri, C. Koroglu, R. Islam, R.A. Iglesias, K. Saraswat, E. Pop, Direct measurement of nanoscale filamentary hot spots in resistive memory devices, Sci. Adv. 8 (13) (2022) eabk1514, https://doi.org/10.1126/sciadv.abk1514.

[16] G.A. Illarionov, S.M. Morozova, V.V. Chrishtop, M.-A. Einarsrud, M.I. Morozov, Memristive TiO_2: synthesis, technologies, and applications, Front. Chem. 8 (2020) 724, https://doi.org/10.3389/fchem.2020.00724.

[17] A. Alessio, V. Bonino, T. Heisig, F. Picollo, D. Torsello, L. Mino, G. Martinez-Criado, R. Dittmann, M. Truccato, Functional modifications induced via X-ray nanopatterning in TiO_2 rutile single crystals, Phys. Status Solidi (RRL) Rapid Res. Lett. 15 (10) (2021) 2100409, https://doi.org/10.1002/pssr.202100409.

[18] L. Mino, V. Bonino, A. Alessio, F. Picollo, A. Kuncser, I. Mercioniu, A.M. Vlaicu, P. Badica, R. Brescia, M. Fretto, K. Goss, R. Dittmann, M. Truccato, Improving the control of the electroforming process in oxide-based memristive devices by X-ray nanopatterning, J. Mater. Chem. C 12 (2024) 11127–11132, https://doi.org/10.1039/d4tc01815j.

[19] L. Mino, V. Bonino, F. Picollo, M. Fretto, A. Agostino, M. Truccato, Tailoring the local conductivity of TiO_2 by X-Ray nanobeam irradiation, Adv. Electron. Mater. 5 (2019) 1900129.

[20] B.L. Henke, E.M. Gullikson, J.C. Davis, X-ray interactions: photoabsorption, scattering, transmission, and reflection at E=50–30000 eV, Z=1-92, At. Data Nucl. Data Tables 54 (2) (1993) 181–342.
[21] W.J. Lin, D. Li, Y.T. Su, H.B. Shi, L. Wang, X.Y. Cao, Y. Meng, H.W. Zhao, Nondestructive visualization of interfacial conducting inhomogeneities in memristive oxides by electroluminescence, Adv. Mater. Interfaces 8 (2021) 2001617, https://doi.org/10.1002/admi.202001617.
[22] N. Jiang, D. Su, J.C.H. Spence, Determination of ti coordination from pre-edge peaks in ti k -edge XANES, Phys. Rev. B 76 (21) (2007) 214117, https://doi.org/10.1103/PhysRevB.76.214117.
[23] G.A. Tompsett, G.A. Bowmaker, R.P. Cooney, J.B. Metson, K.A. Rodgers, J. M. Seakins, The Raman spectrum of brookite, TiO_2 (Pbca, Z=8), J. Raman Spectrosc. 26 (1) (1995) 57–62, https://doi.org/10.1002/jrs.1250260110.
[24] V. Swamy, B.C. Muddle, Q. Dai, Size-dependent modifications of the Raman spectrum of rutile TiO_2, Appl. Phys. Lett. 89 (16) (2006) 163118, https://doi.org/10.1063/1.2364123.
[25] J. Dhanalakshmi, S. Iyyapushpam, S.T. Nishanthi, M. Malligavathy, D. Pathinettam Padiyan, Investigation of oxygen vacancies in ce coupled TiO_2 nanocomposites by Raman and PL spectra, Adv. Nat. Sci Nanosci. Nanotechnol. 8 (1) (2017) 015015, https://doi.org/10.1088/2043-6254/aa5984.
[26] D. Carta, G. Mountjoy, A. Regoutz, A. Khiat, A. Serb, T. Prodromakis, *x*-ray absorption spectroscopy study of TiO_{2-x} thin films for memory applications, J. Phys. Chem. C 119 (8) (2015) 4362–4370, https://doi.org/10.1021/jp511739h.
[27] J.P. Strachan, J.J. Yang, R. Muenstermann, A. Scholl, G. Medeiros-Ribeiro, D. R. Stewart, R.S. Williams, Structural and chemical characterization of TiO_2 memristive devices by spatially-resolved NEXAFS, Nanotechnology 20 (48) (2009) 485701, https://doi.org/10.1088/0957-4484/20/48/485701.
[28] G. Guisbiers, O. Van Overschelde, M. Wautelet, Theoretical investigation of size and shape effects on the melting temperature and energy bandgap of TiO_2 nanostructures, Appl. Phys. Lett. 92 (2008) 103121, https://doi.org/10.1063/1.2897297.
[29] A.C. Breeson, G. Sankar, G.K.L. Goh, R.G. Palgrave, Rutile to anatase phase transition induced by n doping in highly oriented TiO_2 films, Phys. Chem. Chem. Phys. 18 (2016) 24722–24728.
[30] A. Medvids, S. Varnagiris, E. Letko, D. Milcius, L. Grase, S. Gaidukovs, A. Mychko, A. Pludons, P. Onufrijevs, H. Mimura, Phase transformation from rutile to anatase with oxygen ion dose in the TiO_2 layer formed on a ti substrate, Mater. Sci. Semicond. Process 106 (2020) 104776.
[31] T. Potlog, M. Dobromir, D. Luca, P. Onufrijevs, A. Medvids, A. Shamardin, Rutile to anatase phase transition in TiO_2:Nb thin films by annealing in H_2 atmosphere, Curr. Appl. Phys. 16 (2016) 826–829.
[32] Seul Ah Kim, Sk. Khaja Hussain, Muhammad A. Abbas, Jin Ho Bang, High-temperature solid-state rutile-to-anatase phase transformation in TiO_2, J. Solid State Chem. 315 (2022) 123510.
[33] Sivakumar Aswathappa, Lidong Dai, Sahaya Jude Dhas Sathiyadhas, Raju Suresh Kumar, Mowlika Varadhappa Reddy, Acoustic shock Wave-Induced rutile to anatase phase transition of TiO_2 nanoparticles and exploration of their unconventional thermodynamic structural transition path of crystallization behaviors, Inorg. Chem. 63 (2024) 17043–17055, https://doi.org/10.1021/acs.inorgchem.4c02723.
[34] H.L. Ma, J.Y. Yang, Y. Dai, Y.B. Zhang, B. Lu, G.H. Ma, Raman study of phase transformation of TiO_2 rutile single crystal irradiated by infrared femtosecond laser, Appl. Surf. Sci. 253 (2007) 7497–7500, https://doi.org/10.1016/j.apsusc.2007.03.047.
[35] E. Dauksta, A. Medvids, P. Onufrijevs, M. Shimomura, Y. Fukuda, K. Murakami, Laser-induced crystalline phase transition from rutile to anatase of niobium doped TiO_2, Curr. Appl. Phys. 19 (2019) 351–355, https://doi.org/10.1016/j.cap.2018.12.018.